International Journal of Multiphase Flow 199 (2026) 105700

Contents lists available at ScienceDirect

International Journal of Multiphase Flow

journal homepage: www.elsevier.com/locate/ijmulflow

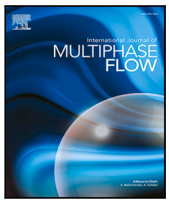

Research Paper

Shock-wave propagation and gas phase growth in droplets deviating from sphericity

Othonas Valeras [a,*], Andreas Papoutsakis [b], Sotirios Damianos [c], Manolis Gavaises [b,c]

[a] Otto von Guericke University Magdeburg, Germany
[b] University of Hertfordshire, UK
[c] City St George University London, UK

ARTICLE INFO

Keywords:
Cavitation
Shock propagation
Compressible multiphase flows

ABSTRACT

In this paper we present a numerical study of supersonic wave propagation in water droplets with shapes deviating from sphericity; uniformly distributed gas nuclei are assumed to be present in the droplet volume, which are subjected to growth under the influence of the passing shockwave. A homogeneous compressible mixture model is utilized together with a finite-rate relaxation approach for the liquid–gas interfacial dynamics, and validated against experimental results. The effect of varying deformation for a range of nominal droplet diameters and for Mach numbers based on the axial velocity ranging from M = 2.4 to 4.4 is reported. The results reveal that as the examined deformed droplet shapes have a shorter length in the direction of the impacting shockwave, gas phase expansion is advanced and reaches higher volume fractions. Additionally, the effect of coherent liquid-aid interfacial structures in the form of harmonic surface disturbances attributed resembling Kelvin–Helmholtz (KH) instabilities is examined. The presence of those surface disturbances lead to multiple wave reflections and wave superpositions that give rise to further amplification of pressure and stronger gas-expansion effects.

1. Introduction

Shock-droplet interactions occur in a wide range of applications at a variety of operational conditions from, ranging from high speed aerodynamic flows (Xiong et al., 2024) and supersonic flight (Gobyzov et al., 2020), atmospheric reentry vehicles (Forehand et al.), to fuel injectors for aircraft engines (Ando, 2010) and liquid rocket engines. Several numerical studies have been conducted, capturing droplet breakup under these conditions. In Nykteri and Gavaises (2021) it was shown that droplet breakup under the shear-induced entrainment regime is dominated by primary and secondary stripping, exhibiting post-shock flow and micro-scale structures cascading to mist formation and secondary droplet sizes. Kelvin–Helmholtz (KH) and Rayleigh–Taylor (RT) instabilities play a central role in droplet deformation and breakup under high-speed aerodynamic or shock-loading conditions. KH instabilities, driven by shear at the gas–liquid interface, promote surface wave growth and ligament formation on the droplet surface. In addition, RT instabilities, arising from acceleration-driven pressure gradients, can pierce the droplet and provide an additional break-up mechanism by triggering multibag-type breakup modes. Many studies (selectively Zhang et al., 2021; Sharma et al., 2021; Dorschner et al., 2020) have shown that these instabilities govern distinct mechanisms of droplet aerobreakup and ligament shedding in high-speed flows and shock-droplet interactions. In the early stages of the shock-droplet interactions, gas nuclei expansion-pseudocavitation can occur (Sembian et al., 2016; Kyriazis et al., 2018; Biasiori-Poulanges and El-Rabii, 2021). The entrapment of air in the form of air bubbles has been highlighted is several studies and can be observed in configurations of rain droplets which can capture and entrap air bubbles during high-speed interactions, with the entrapment dynamics depending on droplet size ratios and Weber numbers (Goyal et al., 2020).

Biasiori-Poulanges and El-Rabii (2021) used ray-tracing to study how acoustic waves propagate inside droplets; they showed that wave focusing can create sharp cusp-like features on the droplet interface shapes in the wavefront. Xu et al. (2023) provided a theoretical model that describes the interaction between the impacting waves and the droplet, and derived the governing/descriptive equations for their form, which were further utilized to study the evolution of planar and cylindrical shocks. In their analysis it was established that that converging shocks make low-pressure regions more pronounced and increase pressure oscillations, thus, raising the chance of nuclei-cavitation. Subsequently, Xiong et al. (2024) improved these models by means of

* Corresponding author.
E-mail address: othonas.valeras@ovgu.de (O. Valeras).

https://doi.org/10.1016/j.ijmultiphaseflow.2026.105700
Received 21 October 2025; Received in revised form 5 February 2026; Accepted 12 March 2026
Available online 24 March 2026

employing an Eulerian multiphase solver with ray-tracing and indicating that the point of the lowest negative pressure (NPP) does not necessarily coincide with the geometric focus of the wave, especially when there are large differences in propagation speed between the gas and liquid phases. This divergence highlights the complex coupling between refraction-driven focusing and phase-dependent acoustic impedance.

Towards modeling the effect of the entrapped air in the compressibility characteristics of liquids, Biasiori-Poulanges and Schmidmayer (2023) developed a multi-material approach that explicitly includes heterogeneous cavitation by modeling the growth of pre-existing nuclei through a relaxation-type phasic interaction. Their results showed that simplified pressure-equilibrium assumptions tend to overestimate the extent and intensity of cavitation. Building on this, Schmidmayer and Biasiori-Poulanges (2023) demonstrated that nuclei-cavitation is less likely to occur in spherical droplets than in cylindrical water columns and identified distinct regimes of cavitation intensity depending on shock strength. Specifically, they found that bubble growth changes from exponential to linear as the axial Mach number exceeds 4.38, corresponding to a transition of the transmitted shock front from concave to convex. Complementary to these findings, Jiao et al. (2024) investigated how the geometry of internal gas cavities, such as their size and eccentricity, affects the resulting wave dynamics, jet formation, and cavity collapse, employing thermodynamically consistent real-fluid models. Despite such progress, high-fidelity three-dimensional studies remain limited. Forehand et al. (2023) performed one of the few 3D investigations using a volume-of-fluid (VOF) solver and compared two mass-transfer formulations, showing enhanced diffusion in spherical configurations.

In our recent study (Damianos et al., 2026) the effect of nuclei gas fraction on wave propagation, its attenuation and nuclei-cavitation formation was reported and validated against experimental data; the study indicated the critical role of gas fraction on wave propagation, the intensity of the gaseous phase expansion, the mixture speed of sound and the diffusion of the transmitted shock front. As a follow-up form this work, we have considered the effect of droplet shapes deviating from sphericity; such effects are absent from the literature, where only spherical droplets or cylindrical liquid columns have been reported. The present study examines the early stages of shock–droplet interactions, as typically occurs, for example, in rain droplets exposed to such shocks.

The droplet shapes studied in this work have been approximated as an oblate spheroid; relevant shapes have been adopted from the early studies of Beard and Chuang (1987) and Wang (1982) where the equilibrium and mathematical description of deformed raindrops and conical hydrometeors under aerodynamic and hydrostatic pressure balance was investigated. Beard and Chuang (1987) derived the equilibrium raindrop shapes by imposing, the coupling the internal hydrostatic pressure with the external aerodynamic pressure and solving the resulting Laplace equations they derived the droplet shape coefficients as functions of the drop diameter. Wang (1982) formulated a parametric conical equation to represent axisymmetric hydrometeors, allowing direct computation of their cross-sectional area and volume. Later, Thurai et al. (2007) refined these shape models using two-dimensional video disdrometer (2DVD) measurements, confirming the deviation of large drops from oblate spheroids and expressing the measured contours through an approximation-function, where the coefficients depend on the equivolumetric spherical diameter.

Moreover, in an effort to explore more realistic droplet-air interfaces where instabilities develop due to the relative velocity, we have imposed single-mode harmonic distortions with varying amplitudes; the effect of multiple combinations of maximum amplitudes and wavelengths has been explored and the effects are compared against the results obtained for undistorted droplets of the same size and exposed to the same incident Mach numbers.

The outline of this paper is as follows. Section 2 introduces the physical cases investigated and discusses the phenomenology of the deformed droplets considered. Section 3 analyses the simulation results across varying droplet shapes and Mach numbers, highlighting their influence on pressure dynamics and gas phase expansion and providing a critical reflection of our results to the literature. Complementary information for the model description and validation against experimental data have been reported in our recent work (Damianos et al., 2026); they are included here as appendices for completeness.

2. Case description

All cases studied, involve the interaction between an axisymmetric water droplet with a uniform gas phase distribution and varying geometry shapes, and an incident shock wave with supersonic axial Mach number. As the shock wave interacts with the droplet interface (see Fig. 1) the incident wave is transmitted through the droplet and at the same time a pressure wave is reflected upstream due to the high acoustic impedance ratio between the two materials i.e. the air and the water. The transmitted pressure wave creates an upstream high pressure region, compressing the gas phase entrapped in the droplet, thus, reducing its volume fraction (Fig. 1b). As it reaches the rear of the droplet (Fig. 1c), it reflects backwards as an expansion wave, and due to the concave shape of the droplet, it converges near the rear reducing the local pressure. If the transmitted pressure wave is sufficiently strong, the generated suction region forces the gas phase to expand rapidly, increasing its volume fraction (depicted in Fig. 1(e). This constitutes a cavitation-like expansion driven solely by gas dynamics, without phase change. **After the completion of the convergence of the transmitted wave, it diverges by shaping a horsehoe** (Fig. 1f).

3. Case setup

All cases involve an axisymmetric domain, in which a shock wave, modeled by Rankine–Hugoniot relations (Toro, 2009) travels across air (gaseous phase) in the axial direction and interferes with a water droplet (liquid phase) containing a uniform amount of gas nuclei with a volume, $a_{air} = 10^{-6}$. The case geometry is identical to the one presented in the experimental case outlined in Fig. 16(a) (see Appendix); the domain dimensions scale with the droplet diameter D as $3D \times 1.5D$. As already mentioned, for the initialization of the droplet geometry, several models have been proposed over the years (Wang, 1982; Beard and Chuang, 1987; Lim, 2006). In the current work, the mathematical relations of Thurai et al. (2007) have been used, which provide the best-fitted equation to the most probable contour of drop shape based on their artificial rain experiment. The droplet shapes from their experiment showed good agreement with the shape model of Beard and Chuang (1987), and their expressions are as follows:

$$y(x) = c_1\sqrt{1-\left(\frac{x}{c_2}\right)^2}\left[\cos^{-1}\left(\frac{x}{c_3 c_2}\right)\right]\left[c_4\left(\frac{x}{c_2}\right)^2+1\right], \quad -c_2 \le x \le c_2 \tag{1}$$

where x and y are the Cartesian coordinates and the parameters c_1, c_2, c_3 and c_4 were fitted to obtain the mean dependence on the equivolumetric sphere diameter (D_{eq} in mm), given by

$$c_1 = \frac{1}{\pi}(0.02914 D_{eq}^2 + 0.9263 D_{eq} + 0.07791) \tag{2}$$

$$c_2 = -0.01938 D_{eq}^2 + 0.4698 D_{eq} + 0.09538 \tag{3}$$

$$c_3 = -0.06123 D_{eq}^3 + 1.3880 D_{eq}^2 - 10.41 D_{eq} + 28.34 \tag{4}$$

$$c_4 = \begin{cases} -0.01352 D_{eq}^3 + 0.2014 D_{eq}^2 \\ \quad -0.8964 D_{eq} + 1.226 & \text{for } D_{eq} > 4 \text{ mm} \\ 0 & \text{for } 1.5 \text{ mm} \le D_{eq} \le 4 \text{ mm} \end{cases} \tag{5}$$

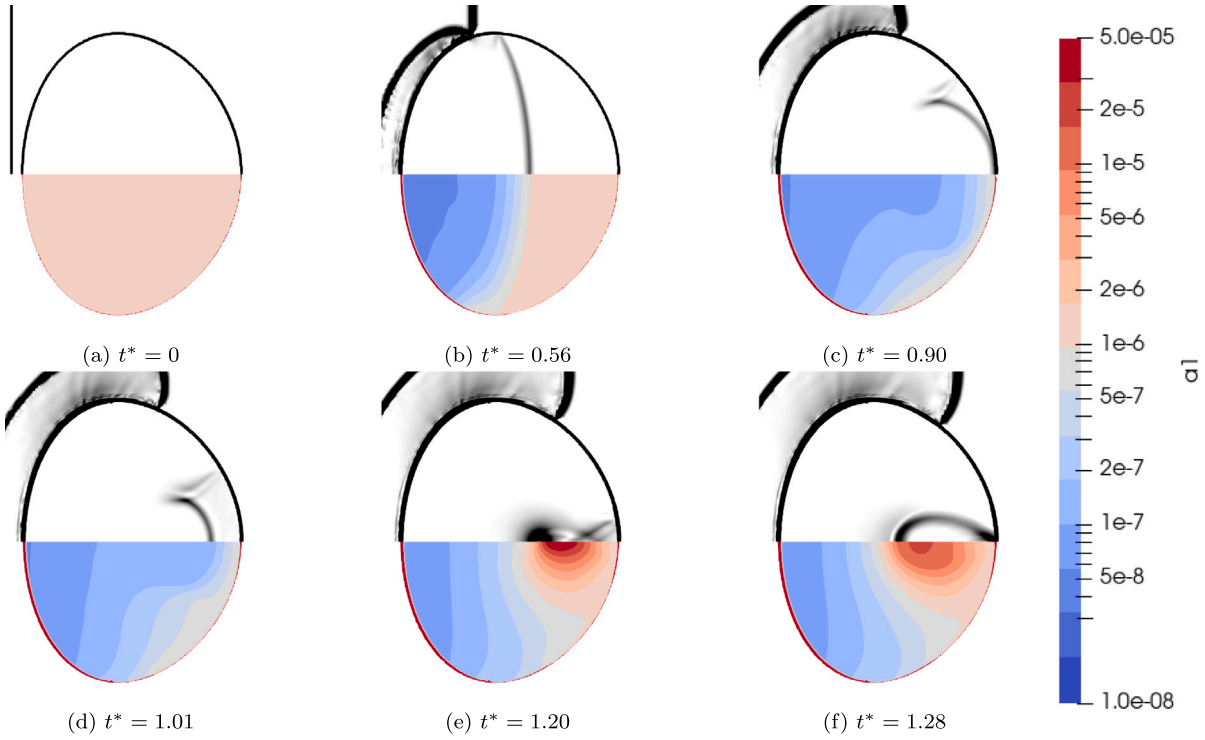

Fig. 1. Wave propagation inside a deformed droplet at six normalized time instants $t^* = D_{eq}/C$ (where C is the speed of sound and D_{eq} is the volumetric equivalent diameter) the density gradient is shown at the top half of each figure, visualizing the wave fronts. The corresponding gaseous volume fraction profile is presented at the bottom half in each snapshot.

Generated droplet shapes with equivalent diameter $D_{eq} = 2, 3, \ldots, 8$ mm are shown in Fig. 2. As the diameter increases, the droplet is deformed from a spherical shape into an oblate spheroid with decreasing axis ratio. As it can be seen, all examined droplet shapes have the points of largest curvature below the center horizontal line and a flatted region around the vertical axis.

In droplets whose interface is exposed to sheer flow with the surrounding air, there exist infinite surface wave patterns, interfering constructively and destructively. To evaluate the effect of such exact distorted droplet shapes on the wave dynamics and gas phase expansion, a harmonic function has been used with varying amplitude across the droplet's arclength while keeping constant wavelength. Due to the nature of the utilized harmonic functions, the mass is conserved in every distorted shape, meaning equal parts of water are displaced inward and outward from the baseline geometry. The implemented distortion function is the following:

$$\delta r = \delta r(x, s) = A(x) \cdot \sin(2\pi \frac{s}{\lambda}) \tag{6}$$

$$A(x) = A_{\max} \cos(2\pi \frac{x}{4c_2}) \quad \text{amplitude varying with } x \tag{7}$$

$$s = s(x) = \int_{-c_2}^{x} \sqrt{1 + (dy/dx)^2}\, dx \quad \text{arc length} \tag{8}$$

In Fig. 3, a distorted droplet profile is shown alongside its baseline shape, highlighting their geometric differences. Both droplets share an equivalent volumetric diameter of $D_{eq} = 8$ mm.

The perturbation wavelength λ was selected based on the findings of Sharma et al. (2021), which reported substantial discrepancies between experimental measurements and existing models for both Rayleigh–Taylor (RT) and Kelvin–Helmholtz (KH) instabilities. While current analytical models provide reasonable order-of-magnitude estimates for the instability wavelength, they fail to predict its exact value (see Fig. 11 and Table 2 of the cited study).

The Weber number (We) is a dimensionless parameter that characterizes the relative importance of a droplet's inertial forces to its surface tension forces, defined as $We = \frac{\rho_g u^2 D}{\sigma}$, where ρ_g is the gas density, u is the relative velocity between the droplet and the gas, D is the droplet diameter, and σ is the surface tension coefficient.

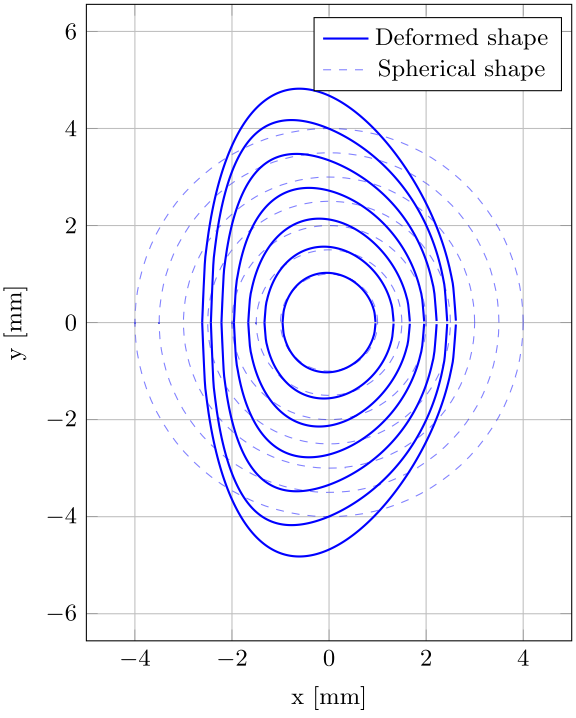

Fig. 2. Droplet shapes for $D_{\text{eq}} = 2, 3, 4, 5, 6, 7, 8$ mm. Dashed circles indicate the corresponding perfect spherical shapes having the same volume as the deformed droplets.

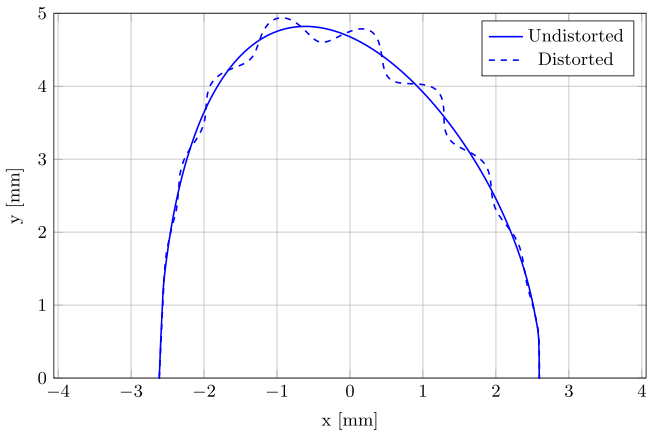

Fig. 3. Comparison of undistorted (dashed) and distorted (continuous) droplet shapes with $D_{eq} = 8$ mm. The distortion shape is generated with $A_{max} = 5\% \cdot D_{eq}$ and wavelength $\lambda = 15\% \cdot D_{eq}$.

For a $D = 2.5$ mm droplet with Weber numbers between 1200 and 12 500, the corresponding measured wavelengths correspond to values between 50 and 250 μm, corresponding to approximately 2%–10% of the droplet diameter. Accordingly, in the present study, wavelengths ranging from 5% to 20% of the droplet diameter were chosen. This wider range helps capture the significant shape deformations and flattening that occur during the initial phases of droplet breakup in the case of KH instabilities. The surface waves amplitudes have been assigned arbitrarily, as in reality, they evolve dynamically during instability growth, which is a process that cannot be simulated with the current framework and is beyond the scope of this work. It is noted that modeling of the complex surfaces generated by RT and KH would require 3D CFD simulations at multiple Weber numbers, with adequate resolution for capturing the developing scales, which are typically beyond the ability of today's HPCs; such a solution could then be then followed simulations such as those presented here, using as initial conditions the predicted surface topologies instead of the superimposed ones utilized. Still, these wavelength and amplitude selections produce surface distortions that qualitatively resemble and cover the range those caused by RT and KH instabilities in deforming droplets. The amplitude attains its maximum value near the equatorial region, corresponding to the location of highest deformation in KH instability growth.

To better resolve the shock wave propagation, an Adaptive Mesh Refinement (Koukas et al., 2023) technique is utilized for all simulations. The base mesh spans a domain of dimensions $3D \times 1.5D$, where D is the nominal droplet diameter, with a grid resolution of 100 cells per D. The geometry and boundary conditions follow the validation case (see Fig. 16(a)), modified to use an axisymmetric wedge mesh rather than 2D, and varying droplet shape and shock Mach number.

To capture the nuclei distribution and the induced gas expansion during the wave propagation inside the droplet, three refinement levels have been tested with a deformed droplet (with no surface instabilities) with diameter $D = 8$ mm and a shock Mach number $M = 2.4$: level 0 (base mesh, no additional refinement, 100 cells per D), level 1 (200 cells per D), level 2 (400 cells per D) and level 3 (800 cells per D). For the droplet-air interface region an additional refinement level 4 is been used, spanning 5 cells on average. This extra refinement helps mitigate numerical diffusion of the interface.

The refinement strategy is illustrated in Fig. 4, which shows the interface of a distorted droplet for the Level 2 refinement case. Refinement levels vary with distance from the droplet boundary, with the highest refinement (Level 4) applied at the interface and progressively coarser refinement away from it.

To quantify gas phase expansion, the total gas volume fraction inside the droplet is used, defined as:

$$V^* = \frac{\int_{V_{droplet}} a_{air}\, dV}{V_{droplet}} \tag{9}$$

where α_{air} is the air volume fraction.

Metrics based on the volume integral of the gas phase volume fraction inside a droplet have been used in previous work (see Schmidmayer and Biasiori-Poulanges (2023) and Biasiori-Poulanges and Schmidmayer (2023)) to quantify gas nuclei expansion and to study shock-induced cavitation in 2D water columns and spherical droplets.

In Fig. 5, the temporal variation of the total gas volume fraction is plotted against the non-dimensional time. As clear from this figure, level 2 refinement produces results nearly identical to level 3. Thus, all simulations have been therefore performed utilizing 2 levels of mesh refinement, which offers a good balance between accuracy and computational cost. For the interface region in droplets with and without surface instabilities, 3 and 4 levels of refinement, correspondingly, have been used to mitigate numerical diffusion and achieve clearer visualization.

4. Results and discussion

4.1. Deformed vs. spherical droplet

In the first case, two droplet geometries are examined with the same equivalent diameter $D_{eq} = 4$ mm: a perfect spherical droplet and a deformed-shaped one. The pressure shock is moving with Mach number $M = 4.0$.

In Fig. 6, results are presented for the temporal variation of total gas volume fraction V^* (Eq. (10)) inside the droplet versus the normalized time t^* (Eq. (9)).

In the deformed droplet case, **the bubble cloud maximum volume** is observed earlier compared to the spherical droplet and reaches higher intensity. More specifically, the first peak is reached in the deformed droplet case at $t^* = 1.15$ with a maximum value $V^* = 1.52 \times 10^{-4}$ and at $t^* = 1.30$ with $V^* = 0.58 \times 10^{-4}$ in the spherical droplet case. This corresponds to a positive difference of 172% with respect to the value reached in the spherical droplet case. The shorter time required for the first pressure peak to be realized, can be explained by the fact that the distorted droplet is compressed in the direction of the moving shock, decreasing the total distance the sound wave needs to travel inside the droplet in order to reach its rear side. The increase of the gas phase expansion, can be attributed to the larger frontal area of the deformed droplet that interacts with the incoming pressure. The increased projected area leads to higher energy transfer into the droplet magnifying the subsequent compression and expansion phenomena.

In Fig. 7, the gas volume fraction and pressure contours for the two simulations are depicted for four time instants. The initial suction region near the rear of the droplet forms earlier in the deformed-shape droplet, visible in the pressure distribution at $t^* = 0.825$, resulting from its compressed frontal geometry. This expansion of the suction region, which precedes the gas volume fraction growth, is more extensive in the deformed droplet, as evidenced by comparing pressure distributions at $t^* = 1.050$ and 1.150. Maximum gas phase expansion, occurs earlier in the deformed droplet (near $t^* = 1.150$) and marks greater volume, compared to the spherical case (near $t^* = 1.300$), with the gas volume fraction distributions clearly highlighting this temporal shift.

4.2. Effect of surface instabilities

To evaluate the influence of surface disturbances on the interface of the deformed-shaped droplet, a test case of two $D_{eq} = 8$ mm drops has been simulated, with a wave-shape disturbance modeled by a function as seen in expression (6). The maximum amplitude and wavelength are

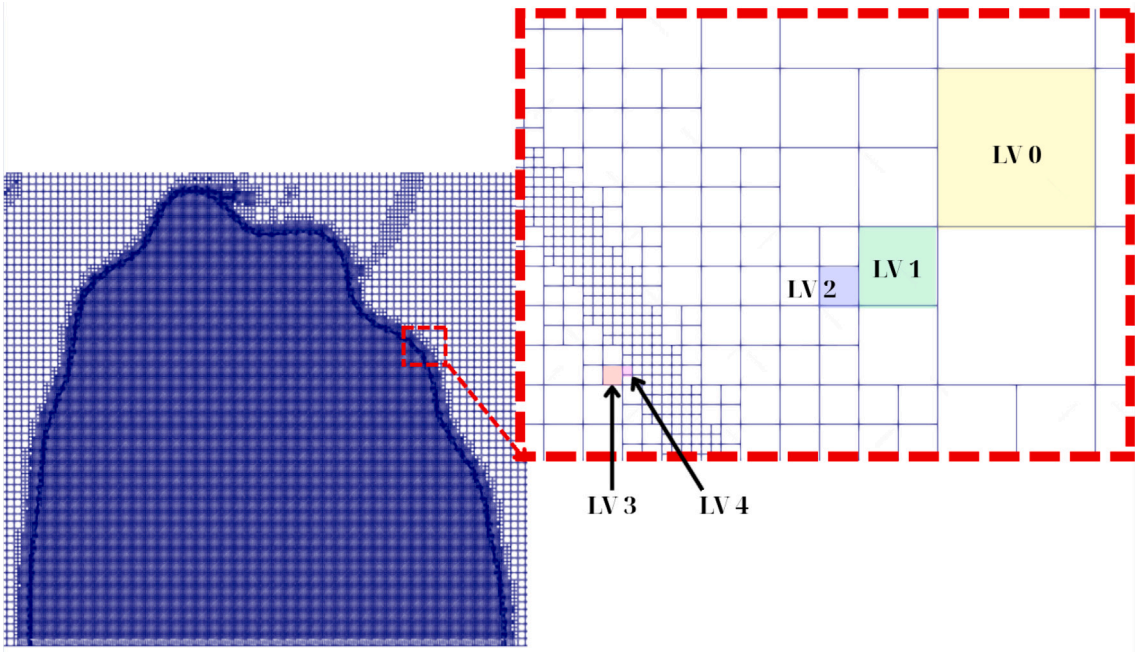

Fig. 4. Mesh refinement for the distorted droplet; non-refined, level 0 cell, is shown with yellow, level 1 with green, level 2 with blue, level 3 with pink and level 4 with light purple. (For interpretation of the references to color in this figure legend, the reader is referred to the web version of this article.)

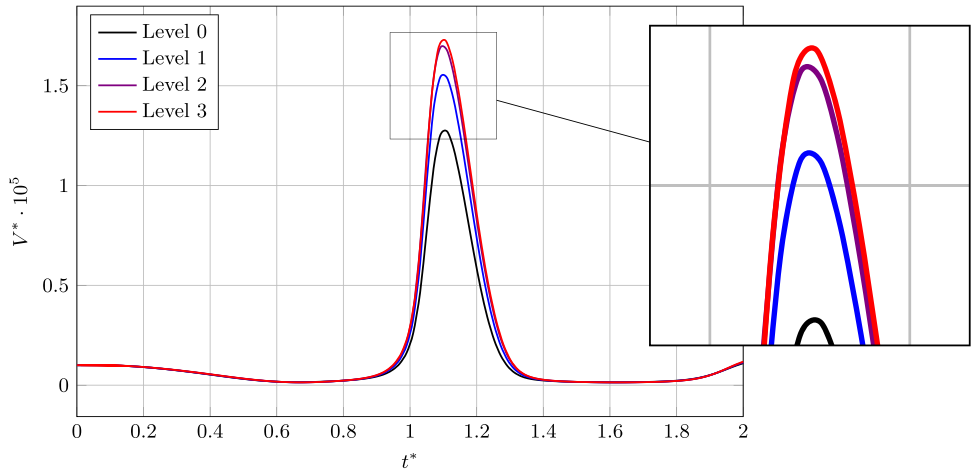

Fig. 5. Effect of mesh refinement on temporal variation of cumulative gas volume fraction for the deformed droplet [D_{eq} = 8 mm, incident shock Mach number M = 2.4].

chosen arbitrarily and expressed as fractions of D_{eq}: $A_{max} = 5\% \cdot D_{eq}$ and $\lambda = 10\% \cdot D_{eq}$. The Mach number is set to $M = 4.4$.

The propagating waves, visualized using the density gradient and pressure contours, are presented in Fig. 8. Results for five time instants are shown; two of them are close to the first interaction of the external pressure wave with the droplet ($t^* = 0.11$ and $t^* = 0.39$) and three instants near **the time of the transmitted wave divergence** ($t^* = 1.18$, 1.24, and 1.29). Initially ($t^* = 0.11$), no remarkable difference can be observed, as the compression wave has not traveled sufficiently inside the droplet, although small differences in density contours are visible, and a small expansion area is created behind the shock (seen in light blue colors). These regions are expected to occur since the distortion itself includes a family of pocket regions where expansion waves are generated after the reflection of the pressure wave. As the main wave propagates further ($t^* = 0.39$) and passes by these pockets, multiple wave are created. These waves interfere constructively and destructively, changing the initial pressure profile and creating areas of higher and lower densities compared to the baseline profile of the undistorted droplet.

As observed in the contours for $t^* = 1.18$ and $t^* = 1.24$ of Fig. 8, these interfering regions **restrain the convergence of the transmitted pressure wave**. At $t^* = 1.24$, the **diverged expansion wave** has already been generated and is propagating, while in the distorted droplet case the pressure is still building up. By $t^* = 1.29$, the **diverged expansion wave** has also developed for the distorted case.

Focusing more on the regions of wave interference seen in Fig. 8 for $t^* = 0.39$, the time interval $t^* = 0.17–0.34$ is explored further: in Fig. 9, four density contours are depicted at sequential instants. It is observed that during this period, as the main compression wave passes by a distortion lobe, a set of interfering wave fronts is created. The stronger waves are highlighted with dashed lines of different colors. With the same colors, the pockets are numbered, showing the propagation of each wave. These waves induce pressure disturbances that delay the **divergence of the expansion wave and prolong nuclei expansion.**

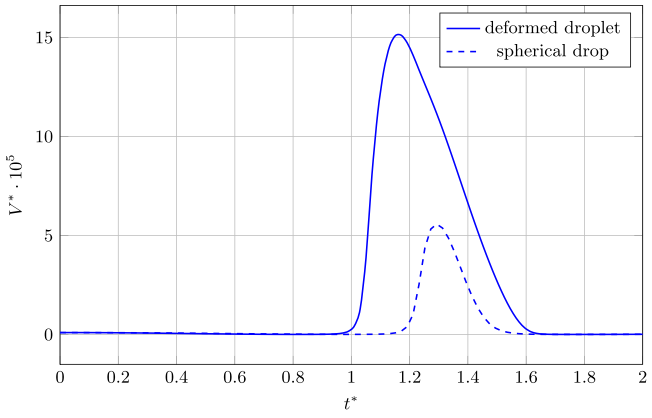

Fig. 6. Comparison of the temporal variation of V^* between the spherical and deformed-shaped droplets [$D_{eq} = 4$ mm and incident shock of $M = 4$].

Table 1
Comparison of maximum gas volume fraction and timing differences. Columns show: (1) Mach number; (2) maximum V^* for undistorted cases; (3) maximum V^* for distorted cases; (4) percentage difference relative to undistorted droplets; (5) t^* at bubble **maximum** V^* for undistorted cases; (6) t^* at bubble **maximum** V^* for distorted cases; (7) time difference between cases.

M	V_u^*	V_d^*	ΔV^* (%)	t_u^*	t_d^*	Δt^*
2.4	1.657e−05	1.552e−05	−6.3%	1.0992	1.0927	−0.0065
2.8	7.078e−05	7.209e−05	+1.8%	1.0860	1.0958	+0.0098
3.2	1.759e−04	1.861e−04	+5.8%	1.1370	1.1674	+0.0304
3.6	3.801e−04	4.014e−04	+5.6%	1.2232	1.2310	+0.0078
4.0	6.936e−04	7.295e−04	+5.2%	1.2833	1.2943	+0.0110
4.4	1.105e−03	1.164e−03	+5.3%	1.3234	1.3346	+0.0112

Their further influence on the gas phase expansion is explored in later sections.

4.3. Effect of incident shock Mach number

The next test case examines the influence of external wave Mach number on the **timing and intensity of the maximum bubble growth** for droplets with $D_{eq} = 8$ mm. The same distortion profile is applied across all cases, with maximum amplitude $A_{max} = 5\% \cdot D_{eq}$ and wavelength $\lambda = 10\% \cdot D_{eq}$. Starting from $M = 2.4$ and increasing to $M = 4.4$ in steps of $\Delta M = 0.4$, the time series of V^* are presented in Fig. 10.

As anticipated due to increased energy transmission and the transition of the transmitted wavefront from concave to convex (Schmidmayer and Biasiori-Poulanges, 2023), enhanced nuclei expansion is observed with increasing Mach number. For the distorted droplets, an increase in the maximum V^* value occurs at all Mach numbers except $M = 2.4$, as shown in Fig. 11. Corresponding results for the characteristic time t^* of the **maximum bubble growth** are presented in Fig. 12, with comprehensive quantitative data provided in Table 1.

The results indicate that for $M \geq 2.8$, the surface distortions delay nuclei expansion and increase its intensity, as evidenced by positive Δt^* and ΔV^* values. In contrast, at $M = 2.4$, **maximum** V^* occurs earlier in the distorted case ($\Delta t^* = -0.0065$) with reduced gas phase expansion intensity ($\Delta V^* = -6.3\%$). Additionally, Fig. 12 reveals a local decrease (acceleration) in t^* when increasing from $M = 2.4$ to $M = 2.8$ for undistorted droplets.

4.4. Effect of maximum surface disturbance wave amplitude

To evaluate the influence of distortion profile on gas phase expansion, two test cases were conducted: varying the maximum amplitude $A_{\max}$ and varying the wavelength λ as a fraction of D_{eq}. For the first case, four droplets were tested with $A_{max} = 15\%$, 20%, 25%, and 30% of the wavelength λ, set to $\lambda = 10\% \cdot D_{eq}$. The incident shock Mach number was set to $M = 2.4$ in all cases.

Table 2
Comparison of maximum vapor volume fraction and timing for varying distortion amplitudes ($\lambda = 10\% \cdot D_{eq}$, $M = 2.4$). Columns show: (1) A_{max} value as fraction of λ; (2) maximum V^*; (3) percentage difference relative to undistorted droplet; (5) t^* at max V^*; time difference between the distorted and the undistorted cases.

A_{max}/λ (%)	V^*	ΔV^* (%)	t^*	Δt^*
Undistorted	1.657e−05	–	1.0992	–
15	1.569e−05	−5.3	1.0946	−0.0046
20	1.550e−05	−6.4	1.0934	−0.0058
25	1.552e−05	−6.3	1.0927	−0.0065
30	1.577e−05	−4.8	1.0931	−0.0062

In Fig. 13, it is observed that for all different distortion profiles, a decrease in both time and V^* occurs, consistent with observations from the previous Mach number variation case. It is also evident that within this range ($15\% \leq A_{max}/\lambda \leq 30\%$), the relative values induce minimal changes in the results. Nonetheless, this decrease in gas phase expansion metrics is not linear. In Table 2 it can be seen that from $A_{max}/\lambda = 15\%$ to 20%, a decrease in expansion intensity is observed; from 20% to 25%, a local minimum is reached observed as nearly identical $V^* - t^*$ graphs in Fig. 13 and close maximum ΔV^* values of −6.4% and −6.3% w.r.t the undistorted droplet, in Table 2; and from 25% to 30%, a relatively steep increase occurs, from −6.3% to −4.8%. The t^* values follow the same variation pattern.

4.5. Effect of surface disturbance wavelength

To evaluate the influence of distortion wavelength on gas phase expansion, four $D_{eq} = 8$ mm droplets have been tested with fixed amplitude $A_{max} = 5\% \cdot D_{eq}$ and varying wavelengths: $\lambda = 5\%$, 10%, 15%, and 20% of D_{eq}. The incident shock Mach number has been set to $M = 2.4$ in all cases.

In Fig. 14, the time evolution of vapor volume fraction reveals distinct behavioral patterns across different wavelengths. The $\lambda = 5\%$ case shows a significant enhancement in gas phase expansion intensity, reaching a maximum V^* value 26.0% higher than the undistorted case, as quantified in Table 3. This increase suggests that very short wavelengths may create constructive interference patterns that amplify rather than suppress bubble formation. The wave fronts, emitted by the multiple distortion pockets are depicted in Fig. 15. For longer wavelengths ($\lambda = 10$–20%) their number declines and the resulting wave forms, reduce expansion intensity, with the $\lambda = 20\%$ case producing the greatest suppression ($\Delta V^* = -9.0\%$).

This does not apply for the difference in characteristic times Δt^*. Increasing λ/D_{eq} from 5% to 20% inflicts a decreasing acceleration, that becomes delay for $\lambda = 20\%$. This can be observed numerically in Table 3, starting from an accelerating value of $\Delta t^* = -0.0054$ for $\lambda = 5\% \cdot D_{eq}$ and reaching a delaying value $\Delta t^* = +0.0067$ for the largest wavelength.

Fig. 15 provides physical insight through density gradient contours at $t^* = 0.5$ (top row) and gas volume fraction visualization at $t^* = 1.05$ (bottom row). The $\lambda = 5\%$ case exhibits extensive constructive wave interference patterns generated by multiple reflection pockets along the droplet surface. Longer wavelengths produce fewer distinct wavefronts due to the reduced number of distortion features. A dotted yellow line marks the 'red' region where $a_{\text{gas}} \geq 0.001$ in the $\lambda/D_{eq} = 5\%$ sub-figure, highlighting the most intense gas phase expansion zone. This region surrounds the corresponding 'red' areas, thus significantly demonstrates the enhanced nuclei expansion observed quantitatively in the $\lambda = 5\%$ configuration.

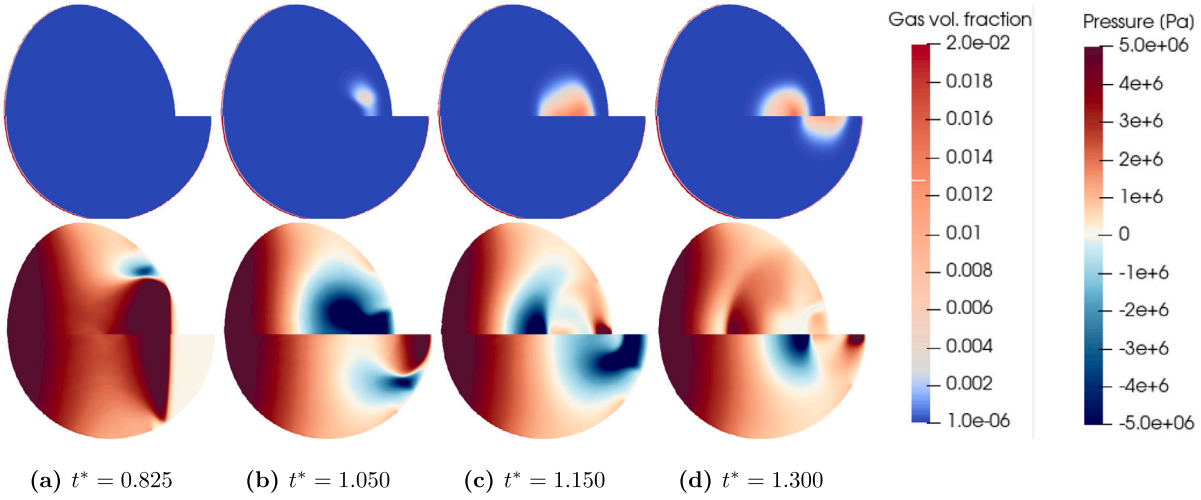

Fig. 7. Comparison of gas volume fraction (top) and pressure (bottom) distribution at four instants for the spherical and real-shaped cases with $D_{eq} = 4$ mm and $M = 4.0$. At the top of each instant, the real-shaped contours are depicted and at the bottom the contours of the spherical droplet.

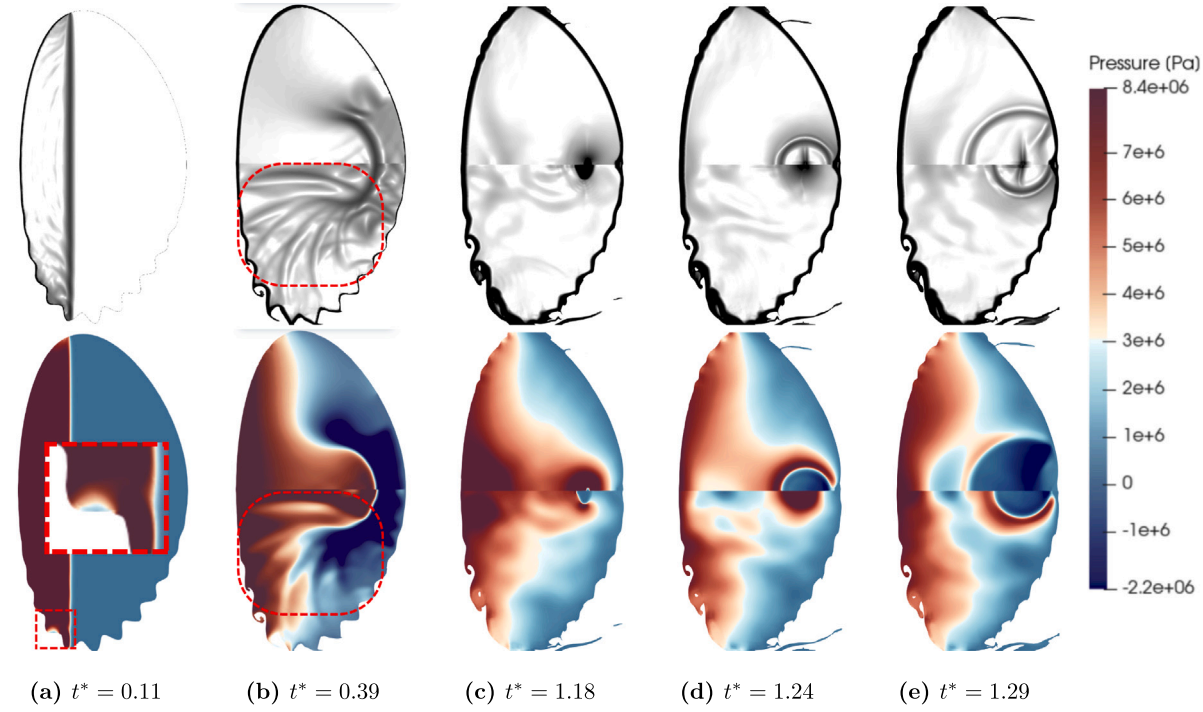

Fig. 8. Comparison of density gradient and pressure distribution for two droplet cases with and without interfacial surface distortions, for the same equivalent diameter $D_{eq} = 8$ mm. Results for five time instants are presented: $t^* = 0.11, 0.39, 1.18, 1.24, 1.29$. In the case of the surface instabilities droplet, additional waves are generated which delay **the divergence of the transmitted expansion wave.**. (For interpretation of the references to color in this figure legend, the reader is referred to the web version of this article.)

Conclusion

This work investigated the dynamics of shock-induced gas phase expansion in deformed droplets using a multiphase compressible CFD model. It demonstrated the relative importance of considering droplet shapes deviating from sphericity and interfacial surface distortions considered via an assumed wave across the periphery of the droplet; these interfacial distortions generate constructive and destructive wave interactions that can either delay or accelerate, intensify or weaken gas nuclei growth, depending on Mach number and distortion characteristics. Increasing shock Mach number generally amplifies gas expansion. Such surface distortions seem to modulate this effect for relative small Mach numbers close to M = 2.4 and intensify gas phase expansion for larger values. Variations in the distortion amplitude showed only minor influence for M = 2.4, whereas wavelength changes proved decisive: very short wavelengths enhanced gas nuclei-pseudocavitation strongly, while longer wavelengths suppressed it.

Overall, these findings underline the sensitivity of gas nuclei expansion to shape irregularities and shock conditions.

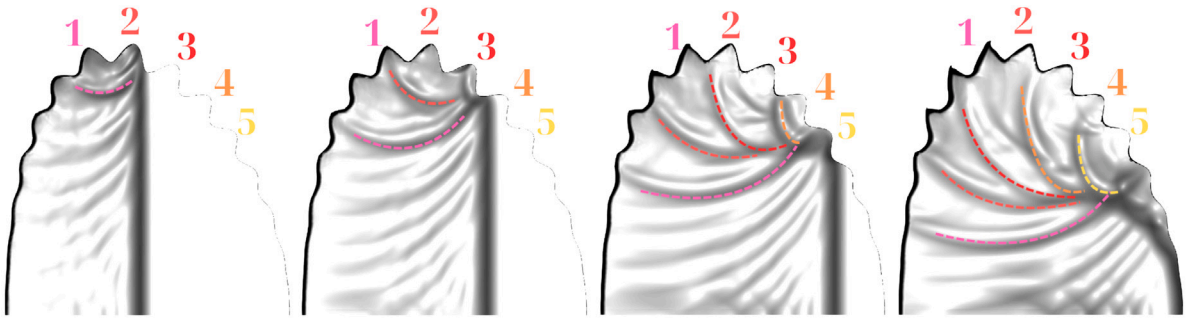

(a) $t^* = 0.17$ (b) $t^* = 0.22$ (c) $t^* = 0.28$ (d) $t^* = 1.34$

Fig. 9. Pressure waves created in the distorted droplet. These create regions of decreased and increased pressure traveling in different directions. The interfering patterns with the highest intensity are marked with dashed lines of different colors, corresponding to the distortion pocket where they were emitted. (For interpretation of the references to color in this figure legend, the reader is referred to the web version of this article.)

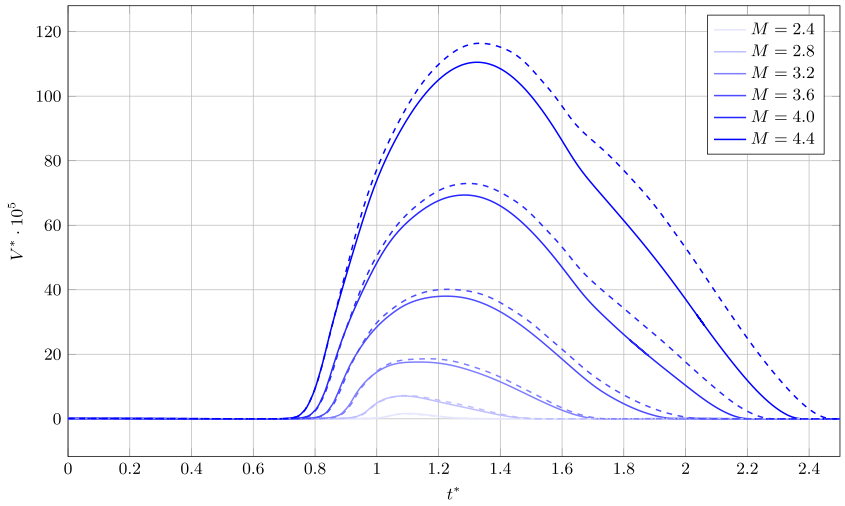

Fig. 10. Time series of vapor volume fraction V^* for Mach numbers ranging from $M = 2.4$ to $M = 4.4$ for both distorted (dashed lines) and undistorted (continuous lines) $D_{\text{eq}} = 8$ mm droplets.

Table 3
Comparison of maximum vapor volume fraction and timing for varying distortion wavelengths ($A_{max} = 5\% \cdot D_{eq}$, $M = 2.4$). Columns show: (1) λ value as fraction of D_{eq}; (2) maximum V^*; (3) percentage difference relative to undistorted droplet; (4) t^* at bubble **maximum expansion**; (5) time difference between the distorted and the undistorted cases.

λ/D_{eq} (%)	V^*	ΔV^* (%)	t^*	Δt^*
Undistorted	1.657e−05	–	1.0992	–
5	2.087e−05	+26.0	1.0938	−0.0054
10	1.552e−05	−6.3	1.0927	−0.0065
15	1.547e−05	−6.7	1.0988	−0.0004
20	1.507e−05	−9.0	1.1059	+0.0067

CRediT authorship contribution statement

Othonas Valeras: Writing – review & editing, Writing – original draft, Visualization, Software, Methodology, Investigation, Formal analysis, Data curation, Conceptualization. **Andreas Papoutsakis:** Writing – review & editing, Validation, Software, Formal analysis. **Sotirios Damianos:** Writing – review & editing, Validation, Software, Methodology, Formal analysis. **Manolis Gavaises:** Writing – review & editing, Supervision, Resources, Project administration, Funding acquisition, Conceptualization.

Declaration of competing interest

The authors declare that they have no known competing financial interests or personal relationships that could have appeared to influence the work reported in this paper.

Acknowledgments

This work was supported by the Horizon Europe MSCA DN projects with acronym SCALE (Industry empowerment to Multiphase fluid dynamics simulations using Artificial intelligence and Statistical methods on modern hardware architectures at Scale), Grant Agreement No. 101120014 and MFLOPS (Multiphase Flow Optimization Strategies with Industrial Applications), Grant agreement 101072851. Additional funding has been received by the UK's Research and Innovation Council (UKRI) through grants EP/Y034686/1 and EP/X041387/1. Views and opinions expressed are however those of the author(s) only and do not necessarily reflect those of the European Union or European Research Executive Agency (REA). Neither the European Union nor the granting authority can be held responsible for them.

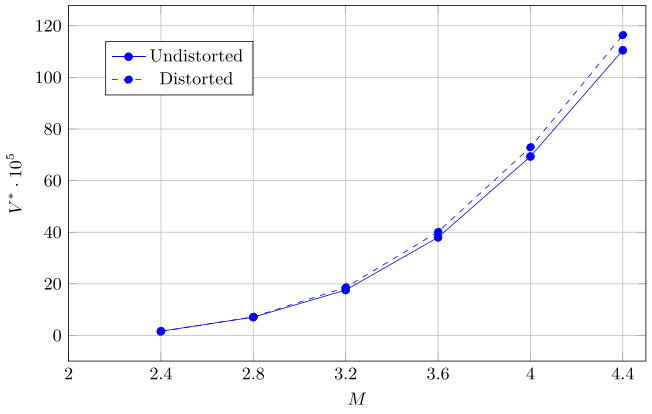

Fig. 11. Maximum V^* versus Mach number for distorted (dashed line) and undistorted (continuous line) droplets. Distortions reduce V^* at $M = 2.4$ but enhance it at higher Mach numbers.

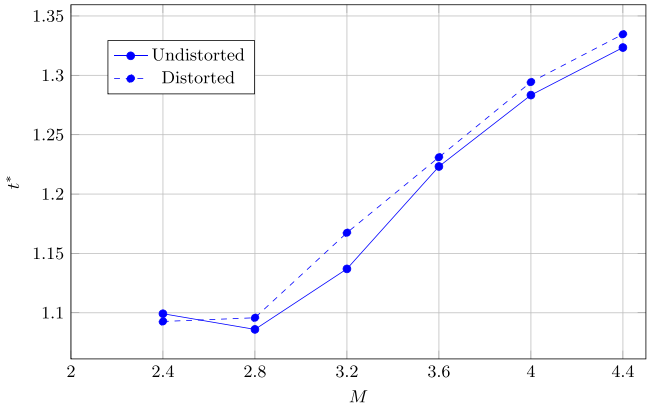

Fig. 12. Bubble time t^* at **max** V^* versus Mach number. Distortions accelerate **maximum expansion** at $M = 2.4$ but delay it at higher Mach numbers.

Appendix

Methodology

Our aim is to model the interaction of a shock wave with a liquid droplet containing entrapped air. For this we have incorporated a computational model presented in Koukas et al. (2023) based on Saurel six-equation model (Saurel et al., 2009) which consists of the phasic continuity and the specific energy equations for each phase, the total momentum conservation equation for the mixture and the transport equation for the volume fraction of the gaseous phase. In addition, the conservation equation for the total energy conservation equation of the mixture is considered. The model accounts for separate pressures for the gas and liquid phases on their interfacial cells, while equilibrium is achieved through a relaxation procedure with a finite relaxation rate (Damianos et al., 2026). This model for diffused interface problems preserves positivity the volume fraction and monotonicity of the mixture sound speed. The governing equations can be written in conservative form as:

$$\frac{\partial \mathbf{U}}{\partial t} + \nabla \cdot \mathbf{F}(\mathbf{U}) + \mathbf{H}(\mathbf{U})\nabla \cdot \mathbf{u} = \mathbf{S}(\mathbf{U}) \tag{10}$$

where $\mathbf{U}$ represents the state vector, $\mathbf{F}$ denotes the flux vector, and $\mathbf{H}$ contains the non-conservative terms, the source term $\mathbf{S}(\mathbf{U})$ handles relaxation processes between phases. The state vectors and flux terms are defined as:

$$\mathbf{U} = \begin{bmatrix} a_1 \\ a_1\rho_1 \\ a_2\rho_2 \\ \rho_{\text{mix}}\mathbf{u} \\ a_1\rho_1 e_1 \\ a_2\rho_2 e_2 \\ \rho_{\text{mix}} E \end{bmatrix}, \quad \mathbf{F} = \begin{bmatrix} a_1\mathbf{u} \\ a_1\rho_1\mathbf{u} \\ a_2\rho_2\mathbf{u} \\ \rho_{\text{mix}}\mathbf{u}\mathbf{u} + P\mathbf{I} - \tau \\ a_1 e_1 \rho_1 \mathbf{u} \\ a_2 e_2 \rho_2 \mathbf{u} \\ (\rho_{\text{mix}} E + P)\mathbf{u} \end{bmatrix}, \quad \mathbf{H} = \begin{bmatrix} -a_1 \\ 0 \\ 0 \\ 0 \\ a_1 P_1 \\ a_2 P_2 \\ 0 \end{bmatrix} \tag{11}$$

The source terms are given by:

$$\mathbf{S} = \begin{bmatrix} \mathcal{P} \\ 0 \\ 0 \\ 0 \\ \mathcal{P}_I \mathcal{P} \\ -\mathcal{P}_I \mathcal{P} \\ 0 \end{bmatrix} \tag{12}$$

a_k is the volume fraction of phase k ($k = 1, 2$ with $a_1 + a_2 = 1$). The phasic density, pressure, and temperature are denoted by ρ_k, P_k, and T_k respectively. The phasic internal energy is $e_k = E_k - \frac{1}{2}\mathbf{u}^2$, where E_k is the total energy of phase k, P_I the interfacial pressure, $\mathcal{P}$ the relaxation operator. Mixture quantities are defined as:

$$\begin{aligned} P &= a_1 P_1 + a_2 P_2 \\ T &= a_1 T_1 + a_2 T_2 \\ \rho_{\text{mix}} &= a_1\rho_1 + a_2\rho_2 \\ E &= a_1 E_1 + a_2 E_2 \end{aligned}$$

where the mixture viscosity is $\mu = a_1\mu_1 + a_2\mu_2$. The interfacial pressure P_I is calculated using acoustic impedances $Z_k = \rho_k C_k$ an estimate in the limit of equal velocities as described in (Saurel et al., 2003):

$$P_I = \frac{Z_1 P_1 + Z_2 P_2}{Z_1 + Z_2} \tag{13}$$

A 2nd order approximation in space and time is used, with a MUSCL approach, while for the calculation of the fluxes in the cell boundaries, the HLLC Riemann solver method is utilized.

The mixture speed of sound, used by HLLC is determined:

$$C = \sqrt{Y_1 C_1^2 + Y_2 C_2^2} \tag{14}$$

where $Y_k = \frac{a_k \rho_k}{\rho_{\text{mix}}}$ is the mass fraction.

The system is closed using the Stiffened Gas (SG) Equation of State for each phase:

$$P_k = (\gamma_k - 1)\rho_k e_k - \gamma_k P_{k,\infty} - (\gamma_k - 1)\eta_k \rho_k \tag{15}$$

$$T_k = \frac{P_k + P_{k,\infty}}{C_{v,k}\rho_k(\gamma_k - 1)} \tag{16}$$

$$C_k = \sqrt{\frac{\gamma_k(P_k + P_{k,\infty})}{\rho_k}} \tag{17}$$

The numerical integration of the system (10) is achieved in three distinct consecutive steps in each timestep:

1. Solve the hyperbolic part of the governing equations while neglecting all source terms.
2. Reinitialize phasic energies to maintain consistency with the total system energy
3. Apply a relaxation procedure to update phasic densities and volume fractions.

The details of the numerical solution can be found in the recently published from the authors (Damianos et al., 2026).

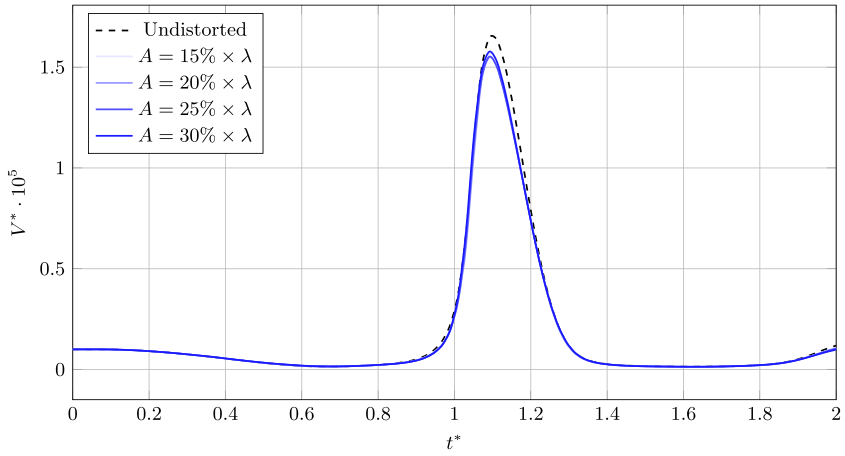

Fig. 13. Normalized vapor volume V^* versus t^* for different amplitude distortions.

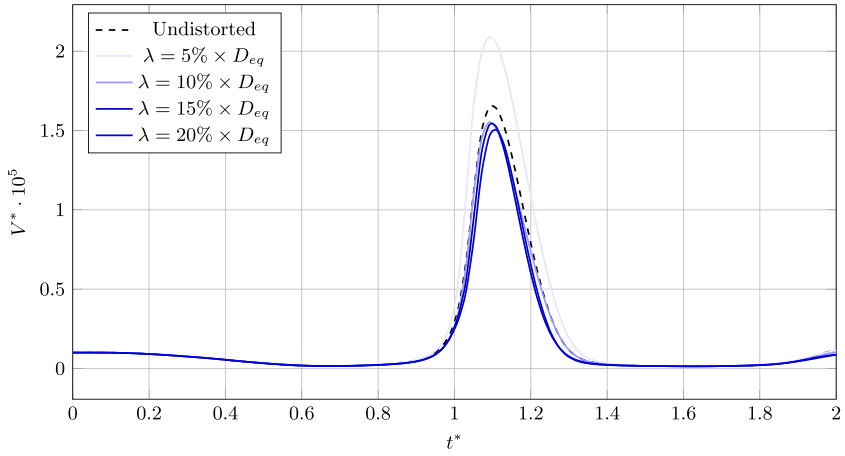

Fig. 14. Temporal evolution of vapor volume fraction for varying wavelength distortions, indicating enhanced expansion at $\lambda = 5\% \cdot D_{eq}$ and progressive suppression at longer wavelengths.

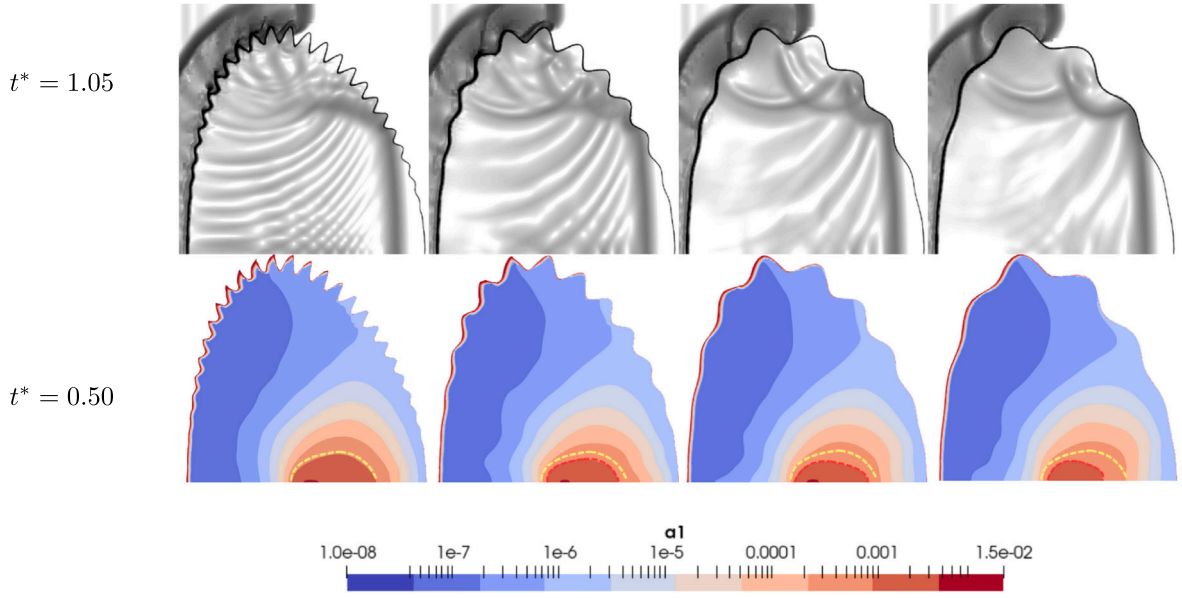

Fig. 15. (Top) Density gradient contours for distorted droplets with different wavelengths at $t^* = 0.50$. (Bottom) Gas volume fraction contours at $t^* = 1.05$. The high gas volume fraction boundary for $\lambda = 5\% D$ (yellow dotted line) is compared with corresponding regions in other cases (red dotted lines). (For interpretation of the references to color in this figure legend, the reader is referred to the web version of this article.)

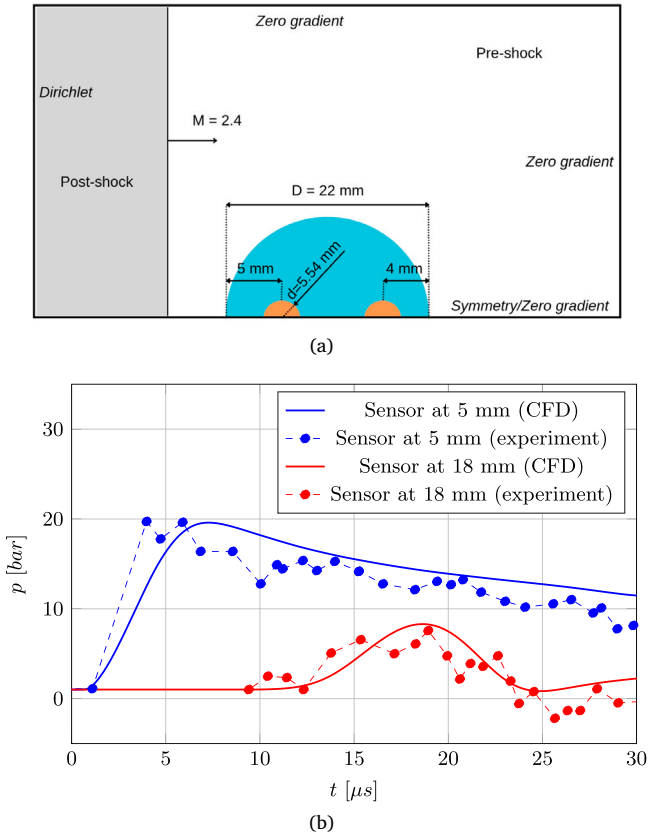

Fig. 16. (a) Representation of the validation case. (b) Pressure contour plots at four time instances during the wave propagation. (c) Comparison of the experimental (dashed lines with points) and the CFD data (smooth lines) for the temporal variation of pressure at the two sensor locations: 5 mm (blue) and 18 mm (red) from the left front of the column. (For interpretation of the references to color in this figure legend, the reader is referred to the web version of this article.)

Model validation

The numerical model was tested using experimental data from Sembian et al. (2016). The numerical setup, shown in Fig. 16(a), consists of a 2D water column with a diameter of $D = 22$ mm. Two pressure sensors, each with a diameter of $d = 5.54$ mm, are placed at distances of 5 mm from the left front and 4 mm from the right rear of the column.

The upstream shock wave with a Mach number of $M = 2.40$ propagates and interacts with the water column, transmitting a pressure wave inside it. The transmitted shock wave first passes the sensor at 5 mm, causing a pressure increase in its vicinity. It then reaches the sensor at 18 mm, where the pressure also rises, but with a lower intensity due to energy dissipation within the column. When the shock wave reaches the rear of the column, it is reflected back as an expansion wave passing the 18 mm sensor, leading to a pressure decrease in the surrounding area.

Using a gas nuclei distributed volume fraction of $a_g = 10^{-3}$ and a finite relaxation factor of $\mu = 0.5$ (see Damianos et al. (2026)), the simulated time series show the best agreement with the experimental data, as presented in Fig. 16(b). The peak pressure deviations from the experimental values are $\Delta P_{5\text{ mm}} = 0\%$ and $\Delta P_{18\text{ mm}} = 5.26\%$. The simulated shock attenuation is $Att_{CFD} = 57.62\%$, which is close to the experimental value of $Att_{exp} = 59.74\%$.

Table 4
Stiffened Gas Equation of State parameters for water and air.

Parameter	Water	Air
P_∞ (Pa)	510 859 269.6	0.0
γ	4.4	1.4
C_p (J/kg K)	2211.769	1006
η (J/kg)	−550 877.242	−327.9746
ρ (kg/m^3)	996	1

Equation of state setup

For the applications in this work, we adopt the Stiffened Gas (SG) EoS:

$$P_k = (\gamma_k - 1)\rho_k^* e_k^* - \gamma_k P_{k,\infty} - (\gamma_k - 1)\eta_k \rho_k \tag{18}$$

where γ_k is the specific heat ratio and $P_{k,\infty}$ and η_k are material-specific constants for phase k, and $C_{v,k}$.

The parameters of the SG EoS are presented in Table 4. The whole domain is initialized with uniform temperature and pressure conditions respectively, $T = 300$ K and $p = 1$ bar.

Data availability

Data will be made available on request.

References

Ando, K., 2010. Effects of Polydispersity in Bubbly Flows (Ph.D. thesis). California Institute of Technology.

Beard, Kenneth V., Chuang, Catherine, 1987. A new model for the equilibrium shape of raindrops. J. Atmospheric Sci. http://dx.doi.org/10.1175/1520-0469(1987)044<1509:ANMFTE>2.0.CO;2, URL https://journals.ametsoc.org/view/journals/atsc/44/11/1520-0469_1987_044_1509_anmfte_2_0_co_2.xml.

Biasiori-Poulanges, L., El-Rabii, H., 2021. Shock-induced cavitation and wave-front analysis inside a water droplet. Phys. Fluids 33 (9), 097104. http://dx.doi.org/10.1063/5.0062922.

Biasiori-Poulanges, L., Schmidmayer, K., 2023. A phenomenological analysis of droplet shock-induced cavitation using a multiphase modeling approach. Phys. Fluids (ISSN: 10897666) 35, http://dx.doi.org/10.1063/5.0127105.

Damianos, Sotirios, Papoutsakis, Andreas, Karathanassis, Ioannis K., Gavaises, Manolis, 2026. Effect of gas nuclei on the primary stage of shock–droplet interaction. Int. J. Multiph. Flow (ISSN: 03019322) 194, 105478. http://dx.doi.org/10.1016/j.ijmultiphaseflow.2025.105478, URL https://linkinghub.elsevier.com/retrieve/pii/S0301932225003532.

Dorschner, Benedikt, Biasiori-Poulanges, Luc, Schmidmayer, Kevin, El-Rabii, Hazem, Colonius, Tim, 2020. On the formation and recurrent shedding of ligaments in droplet aerobreakup. J. Fluid Mech. (ISSN: 14697645) 904, http://dx.doi.org/10.1017/jfm.2020.699.

Forehand, Reed, Nguyen, Khanh C., Anderson, Caroline, Briggs, Sydney M., Berube, Nicolas, Vasu, Subith, Kinzel, Michael P., Grace, Sheryl, Multi-Scale modeling of Shock-Droplet interaction within a shock tube. In: AIAA SCITECH 2023 Forum. http://dx.doi.org/10.2514/6.2023-2304, arXiv:https://arc.aiaa.org/doi/pdf/10.2514/6.2023-2304 URL https://arc.aiaa.org/doi/abs/10.2514/6.2023-2304.

Forehand, R.W., Nguyen, K.C., Anderson, C.J., Shannon, R., Grace, S.M., Kinzel, M.P., 2023. A numerical assessment of shock-droplet interaction modeling including cavitation. Phys. Fluids (ISSN: 10897666) 35, http://dx.doi.org/10.1063/5.0136536.

Gobyzov, Oleg, Ryabov, Michail, Bilsky, Artur, 2020. Study of deformation and breakup of submillimeter droplets' spray in a supersonic nozzle flow. Appl. Sci. 10, 6149. http://dx.doi.org/10.3390/app10186149.

Goyal, Nitin, Shaikh, Javed, Sharma, Atul, 2020. Bubble entrapment during head-on binary collision with large deformation of unequal-sized tetradecane droplets. Phys. Fluids (ISSN: 1070-6631) 32 (12), 122114. http://dx.doi.org/10.1063/5.0029179, arXiv:https://pubs.aip.org/aip/pof/article-pdf/doi/10.1063/5.0029179/19772225/122114_1_online.pdf.

Jiao, Yu, Schmidt, Steffen J., Adams, Nikolaus A., 2024. Effect of gas cavity size and eccentricity on shock interaction with a cylinder at near-critical conditions. Phys. Fluids (ISSN: 10897666) 36, http://dx.doi.org/10.1063/5.0225036.

Koukas, Evangelos, Papoutsakis, Andreas, Gavaises, Manolis, 2023. Numerical Investigation of Shock-Induced Bubble Collapse Dynamics and Fluid-Solid Interactions During Shock-Wave Lithotripsy. Technical Report, City University of London, p. 31.

Kyriazis, N., Koukouvinis, P., Gavaises, M., 2018. Modelling cavitation during drop impact on solid surfaces. Adv. Colloid Interface Sci. 260, 46–64. http://dx.doi.org/10.1016/j.cis.2018.07.002.

Lim, Brian, 2006. Derivation of the Shape of Raindrops. Technical Report, School of Applied and Engineering Physics, Cornell University.

Nykteri, Georgia, Gavaises, Manolis, 2021. Droplet aerobreakup under the shear-induced entrainment regime using a multiscale two-fluid approach. Phys. Rev. Fluids 6, 084304. http://dx.doi.org/10.1103/PhysRevFluids.6.084304, URL https://link.aps.org/doi/10.1103/PhysRevFluids.6.084304.

Saurel, Richard, Gavrilyuk, Sergey, Renaud, François, 2003. A multiphase model with internal degrees of freedom: Application to shock-bubble interaction. J. Fluid Mech. 495, 283–321. http://dx.doi.org/10.1017/S002211200300630X, URL https://www.scopus.com/inward/record.uri?eid=2-s2.0-0344669268&doi=10.1017%2fS002211200300630X&partnerID=40&md5=ab8d032f062f3fe96c983180e151f73f, Cited by: 124.

Saurel, Richard, Petitpas, Fabien, Berry, Ray A., 2009. Simple and efficient relaxation methods for interfaces separating compressible fluids, cavitating flows and shocks in multiphase mixtures. J. Comput. Phys. (ISSN: 10902716) 228, 1678–1712. http://dx.doi.org/10.1016/j.jcp.2008.11.002.

Schmidmayer, K., Biasiori-Poulanges, L., 2023. Geometry effects on the droplet shock-induced cavitation. Phys. Fluids (ISSN: 10897666) 35, http://dx.doi.org/10.1063/5.0151404.

Sembian, S., Liverts, M., Tillmark, N., Apazidis, N., 2016. Plane shock wave interaction with a cylindrical water column. Phys. Fluids 28 (5), 056102. http://dx.doi.org/10.1063/1.4948968.

Sharma, Shubham, Singh, Awanish Pratap, Rao, S. Srinivas, Kumar, Aloke, Basu, Saptarshi, 2021. Shock induced aerobreakup of a droplet. J. Fluid Mech. (ISSN: 14697645) 929, http://dx.doi.org/10.1017/jfm.2021.860.

Thurai, Merhala, Huang, G.J., Bringi, V.N., Randeu, W.L., Schönhuber, M., 2007. Drop shapes, model comparisons, and calculations of polarimetric radar parameters in rain. J. Atmos. Ocean. Technol. (ISSN: 07390572) 24, 1019–1032. http://dx.doi.org/10.1175/JTECH2051.1.

Toro, Eleuterio F., 2009. Riemann Solvers and Numerical Methods for Fluid Dynamics: A Practical Introduction, third ed. Springer Berlin Heidelberg, Berlin, Heidelberg, ISBN: 978-3-540-25202-3, http://dx.doi.org/10.1007/b79761, URL https://link.springer.com/book/10.1007/b79761.

Wang, Pao-Kuan, 1982. Mathematical description of the shape of conical hydrometeors. J. Atmospheric Sci. http://dx.doi.org/10.1175/1520-0469(1982)039<2615:MDOTSO>2.0.CO;2, URL https://journals.ametsoc.org/view/journals/atsc/39/11/1520-0469_1982_039_2615_mdotso_2_0_co_2.xml.

Xiong, Tianheng, Shao, Changxiao, Luo, Kun, 2024. Exploration of shock-droplet interaction based on high-fidelity simulation and improved theoretical model. J. Fluid Mech. (ISSN: 14697645) 988, http://dx.doi.org/10.1017/jfm.2024.472.

Xu, S., Fan, W., Wu, W., Wen, H., Wang, B., 2023. Analysis of wave converging phenomena inside the shocked two-dimensional cylindrical water column. J. Fluid Mech. 962, A14. http://dx.doi.org/10.1017/jfm.2023.48.

Zhang, D., et al., 2021. Aerobreakup of liquid drops by instabilities. Phys. Fluids 33 (8), 082110. http://dx.doi.org/10.1063/5.0056981.